Nano Research

Open Access

Research Article

Construction of N-doped carbon polyhedral encapsulated Co_3O_4-RuO_2 heterostructure for electrocatalytic natural seawater splitting

Yan Lin[1] ✉, Pinxin Liu[1], Zihan Wang[1], Zicheng Liu[1], Jianing Gongye[1], Chao Feng[2] ✉, Yingying Liu[3], Xin Yang[1] ✉, and Yuan Pan[3] ✉

[1] *Shandong Key Laboratory of Integrated Multi-Energy Systems for High Efficiency and Intelligent Operation/College of Energy Storage Technology, Shandong University of Science and Technology, Qingdao 266590, China*
[2] *College of Chemical and Biological Engineering, Shandong University of Science and Technology, Qingdao 266590, China*
[3] *State Key Laboratory of Heavy Oil Processing, China University of Petroleum (East China), Qingdao 266580, China*

Cite this article: *Nano Research*, **2026**, *19*, 94908487. https://doi.org/10.26599/NR.2026.94908487

ABSTRACT: Producing hydrogen from the abundant seawater is very attractive for the sustainable development of hydrogen energy. Rational design and construction of efficient bifunctional catalysts remain a huge challenge. Herein, we report a novel N-doped carbon polyhedral (NCP) encapsulated Co_3O_4-RuO_2 heterostructure (Co_3O_4-RuO_2@NCP) synthesized through a simple "template-assistance-self-assembly-pyrolysis" strategy for both hydrogen evolution reaction (HER) and oxygen evolution reaction (OER) in seawater. The Co_3O_4-RuO_2@NCP catalyst only needs 18 and 250 mV in 1 M KOH, 24 and 260 mV in simulated seawater, 29 and 290 mV in natural seawater to arrive the current density of 10 mA·cm^{-2} for HER and OER, respectively. Meanwhile, only 1.53 and 1.60 V are required to drive 10 mA·cm^{-2} for overall water splitting in 1 M KOH and natural seawater splitting with good stability and high Faraday efficiency. The combined spectroscopy analysis suggested Ru plays a crucial role in this electrolysis process. During the alkaline HER process, Ru^{4+} is partially reduced to Ru(0), and the *in-situ* formed Ru-Co_3O_4 serves as the active center to promote H_2 evolution. While in the alkaline OER process, partial oxidation of Ru occurs, which enhances the electronic coupling with oxygen-containing species and facilitates the OER process. Density functional theory (DFT) calculations also suggested these structural properties optimized the adsorption and activation process of key active species in the electrolysis process, and the electronic interaction between NC and Co_3O_4-RuO_2 enhanced the activity and selectivity in seawater electrolysis under alkaline conditions. This work developed a promising bifunctional electrocatalyst for natural seawater splitting.

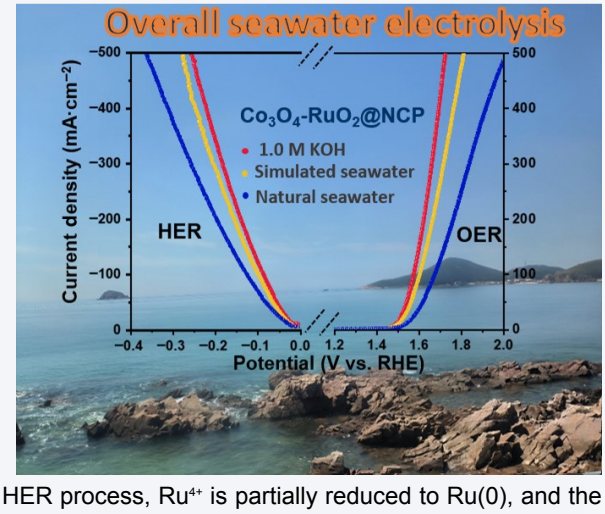

KEYWORDS: metal-organic frameworks, heterostructure, electrocatalysis, natural seawater splitting

1 Introduction

Electrolyzed seawater which accounts for 97% of the total water reserves of our planet for hydrogen production through hydrogen evolution reaction (HER) is extremely attractive. While natural seawater contains electrochemically active ions which would interfere and compete with the water electrocatalysis, one of the challenges is chlorine evolution reaction (CER), which reduced electrolysis efficiency and damaged the long-term stability of the system. Alkaline electrolyte facilitates the selective splitting of seawater [1]. While due to the lack of H^+, HER in alkaline media starts from dissociating H_2O molecules to provide protons, so the adsorption and activation of H_2O molecules is critical for alkaline seawater electrolysis [2]. What is more, the entire water electrolysis reaction includes two half reactions: HER at the cathode and oxygen evolution reaction (OER) at the anode, given the cost reduction and device simplification, integrating the active

Received: September 18, 2025; **Revised:** January 20, 2026
Accepted: January 21, 2026

✉Address correspondence to Yan Lin, linyan09@sdust.edu.cn; Chao Feng, fengchao@sdust.edu.cn; Xin Yang, yangx@sdust.edu.cn; Yuan Pan, panyuan@upc.edu.cn

components of HER and OER into a single nanostructure simultaneously is highly desired.

Researches suggested the oxygen-containing species such as H_2O molecules or OH^- may interact strongly with the oxide surfaces, while these oxygen-containing species are not only key active species for HER but also for OER, which may grant metal oxides (TMOs) the ability to integrate the excellent HER and OER activities simultaneously in alkali [3]. Metal-organic frameworks (MOFs) or their derivatives materials, with their precisely designed structure, high specific surface area, and excellent catalytic performance, provide a promising path for achieving efficient electrocatalytic performance [4, 5]. And MOFs are good precursor to construct TMOs due to the low pyrolysis temperature. Meanwhile, the organic ligands in MOFs can generate conductive carbon layers in the pyrolysis process, which encapsulated oxide particles and improved the conductivity of TMOs. Among them, zeolitic-imidazolate framework (ZIF), such as the low-cost and easily obtainable ZIF-67 containing Co as the metal center is widely applied [6].

Ruthenium (Ru)-based TMOs were recently reported as most promising bifunctional electrocatalyst due to the remarkable catalytic activity and the cheapest price among the Pt-group metal family [7, 8]. And ZIF-67 was good candidate to work as the matrix and stable skeleton to anchored and stabilized Ru species, simultaneously providing the second active metal Co. Herein, a N-doped carbon polyhedral encapsulated Co_3O_4-RuO_2 heterostructure (Co_3O_4-RuO_2@NCP) is synthesized through a simple "template-assistance-self-assembly-pyrolysis" strategy [9, 10]. The Co_3O_4-RuO_2@NCP with 0.9 at.% of Ru shows the best performance. It displayed bifunctional electrochemical activity on HER and OER in 1 M KOH electrolyte, it only needs 18 and 250 mV vs. RHE to arrive the current density of 10 mA·cm^{-2} for HER and OER, more importantly, bifunctional electrochemical activity also can be kept in alkaline simulated seawater (1 M KOH + 0.5 M NaCl) and alkaline natural seawater (1 KOH + natural seawater from the Yellow Sea), Co_3O_4-RuO_2@NCP needs 24 and 29 mV vs. RHE to drive the current density to 10 mA·cm^{-2} for HER, and only 260 and 290 mV vs. RHE were needed to arrive 10 mA·cm^{-2} for OER in alkaline simulated seawater and alkaline natural seawater, exceeding many reported catalysts. Finally, the electrocatalytic performance on full water electrolysis was performed in a two-electrode cell with Co_3O_4-RuO_2@NCP as both cathode and anode, 1.82 and 1.93 V were needed to drive the current density to 100 mA·cm^{-2} in alkali and alkaline natural seawater electrolyte for Co_3O_4-RuO_2@NCP||Co_3O_4-RuO_2@NCP electrode couple, with high Faraday efficiencies, demonstrating high selectivity for water electrolysis even in seawater. X-ray photoelectron spectroscopy (XPS) and valence band (VB) spectra proved the crucial roles of Ru in this electrolysis process. Density functional theory (DFT) calculations revealed the reconstruction of the active sites during electrocatalysis optimized the adsorption and activation process of key active species, and the electronic interaction between N-doped carbon (NC) and Co_3O_4-RuO_2 heterostructure enhanced the electrocatalytic performance for both HER and OER reaction in seawater under alkaline conditions.

2 Results and discussion

2.1 Structure and characterization of Co_3O_4-RuO_2@NCP catalyst

The Co_3O_4-RuO_2@NCP catalyst was synthesized by a novel "template-assistance-self-assembly-pyrolysis" strategy. ZIF-67 and the graphitic carbon nitride (g-C_3N_4) were used to anchor and disperse the Ru metal. The XRD patterns of the samples (Fig. S1 in the Electronic Supplementary Material (ESM)) suggested with the increasing of the Ru amount, the crystal phase transformed from pure phase Co_3O_4 to Co_3O_4-RuO_2 mixed phase. The diffraction peaks at 19.0°, 31.3°, 36.8°, 44.8°, 59.3°, and 65.2° correspond to the (111), (220), (311), (400), (511), and (440) crystal planes of Co_3O_4 (PDF #43-1003), respectively. The diffraction peaks located at 28.0°, 40.6°, and 45.0°, corresponding to the (110), (111), and (210) crystal planes of RuO_2 (PDF #40-1290), respectively (Fig. 1(a)). In addition, all samples have a diffraction peak near 22.0° corresponding to the graphitized carbon (002) crystal plane. Co_3O_4-RuO_2 (synthesized with mole ratio of Ru:Co = 1:1 but no g-C_3N_4), the Co_3O_4@NC

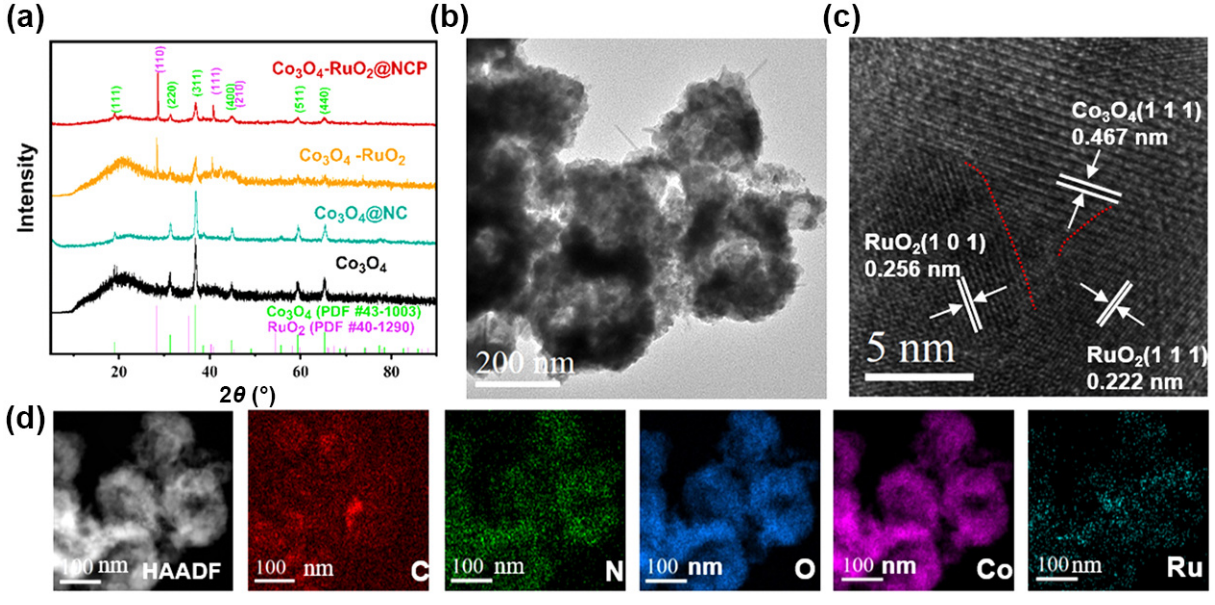

Figure 1 (a) XRD patterns, (b) TEM image, (c) HRTEM image, and (d) HAADF-STEM elemental mapping images of Co_3O_4-RuO_2@NCP.

(synthesized with g-C_3N_4 but no Ru), and the Co_3O_4 (no g-C_3N_4 and Ru) were also constructed for comparison.

There exists morphology difference in the transmission electron microscope (TEM) images. Co_3O_4-RuO_2 shows compact irregular accumulation of particles (Fig. S2(a) in the ESM). Co_3O_4-RuO_2@NCP exhibits a hollow polyhedral structure (Fig. 1(b) and Fig. S2(b) in the ESM), indicating that the dodecahedral structure of ZIF-67 was retained during the pyrolysis process, and the hollow morphology can be attributed to g-C_3N_4, which increases the active surface area befitting the electrocatalytic process [11]. High resolution TEM (HRTEM) of Co_3O_4-RuO_2@NCP (Fig. 1(c)) displayed the distinct lattice spacing of 0.467, 0.256 and 0.222 nm assigned to the (111) crystal plane of Co_3O_4, (101) and (111) crystal planes of RuO_2, the distinct heterointerface can be observed. The high-angle annular dark-field scanning transmission electron microscope (HAADF-STEM) and energy dispersive X-ray spectroscopy (EDX) elemental mapping images (Fig. 1(d)) proved the coexistence of C, N, O, Co and Ru, the dispersion of metal atoms was improved attribute to ZIF-67 framework, and the atomic fraction (at.%) for Ru is 0.9% (Fig. S3 and Table S1 in the ESM). The N_2 adsorption-desorption tests of Co_3O_4-RuO_2@NCP and Co_3O_4-RuO_2 were used to obtain the Brunauer–Emmett–Teller (BET) specific surface area and pore size distributions (Fig. S4 in the ESM). It can be observed that all the isotherms showed type IV [12–15]. The BET specific surface areas for Co_3O_4-RuO_2@NCP and Co_3O_4-RuO_2 are 35.5 and 40.81 $m^2 \cdot g^{-1}$, and the average pore sizes were 24.11 and 17.27 nm, with almost identical pore volumes of 0.23 and 0.22 $cm^3 \cdot g^{-1}$, suggesting the limited impact of g-C_3N_4 on the specific surface area and pore structure.

2.2 Bifunctional electrocatalytic performance in 1 M KOH electrolyte

The electrocatalytic performance of the samples with different amount of Ru was first performed, linear scanning voltammetry (LSV) curves (Fig. S5 in the ESM) for HER and OER in 1 M KOH demonstrated introducing Ru can improve the electrocatalytic activity and Co_3O_4-RuO_2@NCP was most efficient due to the smallest overpotential, thus Co_3O_4-RuO_2@NCP was selected as the target research sample. LSV curves for HER in Fig. 2(a) show that the HER catalytic performance of pure Co_3O_4 and Co_3O_4@NC is poor in 1 M KOH, they need 308 and 288 mV vs. RHE to arrive 10 $mA \cdot cm^{-2}$, respectively. Introducing Ru can significantly improve the HER performance, even without of the assistance of g-C_3N_4 (Co_3O_4-RuO_2 as referred), 54 mV vs. RHE was needed to arrive 10 $mA \cdot cm^{-2}$. The Co_3O_4-RuO_2@NCP only needed 18 mV vs. RHE to reach the current density of 10 $mA \cdot cm^{-2}$, and it exhibited the smallest Tafel slopes (Fig. 2(b)) in 1 M KOH solution (57.6 $mV \cdot dec^{-1}$), suggesting the electrocatalytic reaction rate on Co_3O_4-RuO_2@NCP surface is highly sensitive to the potential change, corresponding to a faster kinetic process, and the reaction mechanism followed the Volmer–Heyrovsky process (Volmer step: $H_2O + e^- = H_{ads} + OH^-$, Heyrovsky step: $H_2O + e^- + H_{ads} = H_2 + OH^-$) [16]. All the electrochemical impedance spectroscopy (EIS) curves (Fig. S6(a) in the ESM) displayed semicircle, but Co_3O_4-RuO_2@NCP showed the smallest diameter, suggesting the smallest charge transfer resistance (R_{ct}), corresponding to the accelerated charge transfer process. Capacitance of the double electric layer (C_{dl}) can be used to estimate the electrochemically active surface area (ECSA) of the catalyst, and the C_{dl} value can be obtained from the cyclic voltammetry curves in non-Faraday potential window (Figs. S7(a)–S7(e) in the ESM), C_{dl} value for Co_3O_4-RuO_2@NCP was 38.22 $mF \cdot cm^{-2}$, which was significantly higher than that of Co_3O_4-RuO_2 (30.3 $mF \cdot cm^{-2}$), Co_3O_4@NC (19.6 $mF \cdot cm^{-2}$) and Co_3O_4 (11.5 $mF \cdot cm^{-2}$), suggesting the higher ECSA of Co_3O_4-RuO_2@NCP.

LSV curve (Fig. 2(c)) for OER showed that the overpotential of Co_3O_4-RuO_2@NCP at 10 $mA \cdot cm^{-2}$ was 250 mV vs. RHE, which was lower than that of Co_3O_4-RuO_2 (268 mV vs. RHE), Co_3O_4@NC (328.8 mV vs. RHE) and Co_3O_4 (374.2 mV vs. RHE), further confirmed that Co_3O_4-RuO_2@NCP also was efficient for electrocatalytic OER. Tafel curves (Fig. 2(d)) showed that the Tafel slope for Co_3O_4-RuO_2@NCP (71.6 $mV \cdot dec^{-1}$) was significantly

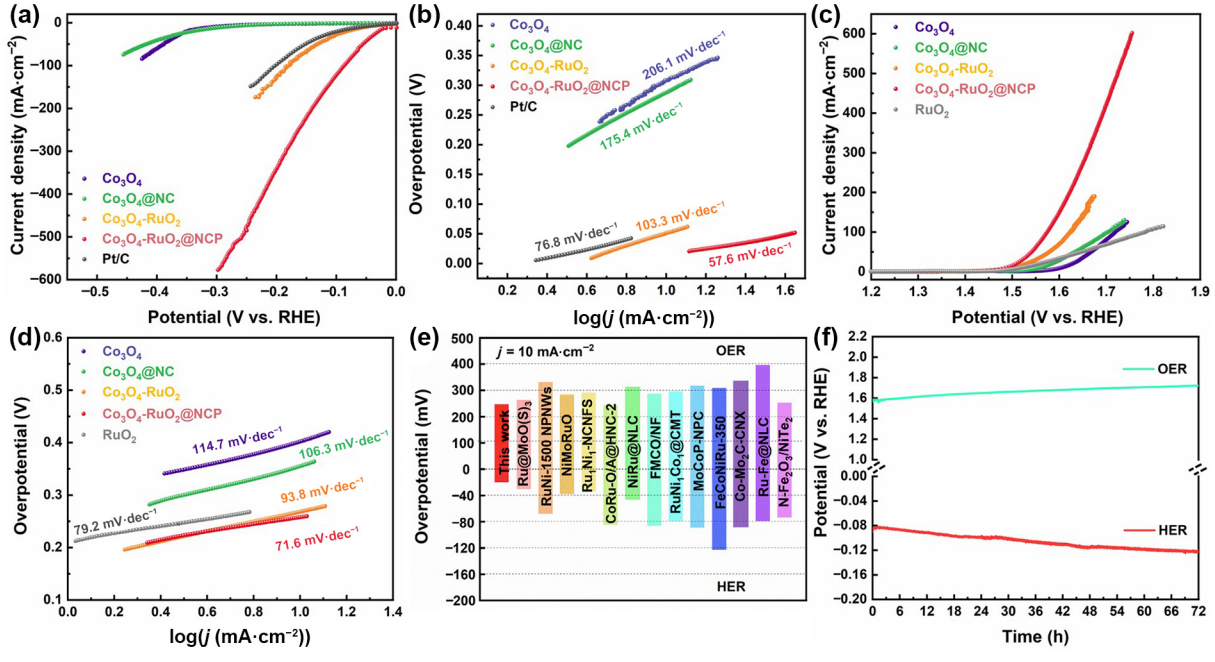

Figure 2 (a) LSV curves and (b) Tafel plots for HER, (c) LSV curves and (d) Tafel plots for OER in 1 M KOH, (e) performance comparison with reported catalyst [17–28], and (f) stability curves.

lower than that of Co_3O_4-RuO_2 (93.8 mV·dec^{-1}), Co_3O_4@NC (106.3 mV·dec^{-1}) and Co_3O_4 (114.7 mV·dec^{-1}), indicating a superior dynamic process on Co_3O_4-RuO_2@NCP. EIS curves (Fig. S6(b) in the ESM) displayed Co_3O_4-RuO_2@NCP had the smallest diameter of a semicircle, suggesting the superior charge transfer capability. As a bifunctional electrocatalyst, the electrocatalytic activity of Co_3O_4-RuO_2@NCP exceeds many reported Ru, Co based catalysts [17–28] (Fig. 2(e)).

In addition, the chrono-potential curves of Co_3O_4-RuO_2@NCP tested continuously for 72 h in 1 M KOH electrolyte were shown in Fig. 2(f), which only showed a slight damage of the potential for both HER and OER, indicating that the Co_3O_4-RuO_2@NCP also has good electrochemical stability.

2.3 Bifunctional electrocatalytic performance in seawater

Producing hydrogen from seawater restarts the legend of "blue energy", which is very attractive for the popularization and sustainable development of hydrogen energy [29]. The HER electrocatalytic performance of the Co_3O_4-RuO_2@NCP was investigated in the alkaline simulated seawater (1 KOH + 0.5 M NaCl) and alkaline natural seawater (1 KOH + natural seawater from the Yellow Sea) (Fig. 3(a)), and the LSV curves (Fig. 3(b)) suggested Co_3O_4-RuO_2@NCP need 24, and 29 mV vs. RHE to drive the current density to 10 mA·cm^{-2} for HER in alkaline simulated seawater and alkaline natural seawater, respectively, showing a slight decrease compared with that in 1 KOH, demonstrating the high catalytic activity can be maintained even in the presence of chloride ions, which is usually challenging for most conventional HER catalysts due to possible corrosion and catalyst poisoning effect [30, 31]. Moreover, the LSV curves almost coincided at lower current densities (≤ 50 mA·cm^{-2}), suggesting other impurities in seawater almost has no influence on the HER electrocatalytic activity at low current densities. Co_3O_4-RuO_2@NCP also shows good OER electrocatalytic activity, 260 and 290 mV vs. RHE were needed to arrive 10 mA·cm^{-2} (Fig. 3(b)). To further assess the practical feasibility of the catalyst in seawater electrolysis, chrono-potential test was performed to assess stability for HER and OER in alkaline natural seawater (Fig. 3(c)). The results showed that the activity can be maintained for at least of 72 h. And inductively coupled plasma atomic emission spectrometry (ICP-AES) was performed to test the dissolved Ru and Co in the seawater electrolyte (Fig. S8 in the ESM), the dissolved amounts of Ru and Co after HER stability test were 4.033 and 5.567 μg·L^{-1}. After OER stability test, the dissolved amount of Ru and Co increased to 76.08 and 18.868 μg·L^{-1}, which can be attributed to the high oxidation potential of anode and the corrosion and coordination of chloride ions, that is inevitable. And the acceptable loss rates demonstrated the robustness of the Co_3O_4-RuO_2@NCP structure.

Two-electrode system tests with Co_3O_4-RuO_2@NCP as both anode and cathode were conducted (Fig. 4(a)) in 1 M KOH and alkaline natural seawater to investigate the performance towards overall water splitting. It suggested Co_3O_4-RuO_2@NCP||Co_3O_4-RuO_2@NCP electrode pair needs 1.53 and 1.60 V to drive the current density to 10 mA·cm^{-2} in 1 M KOH and alkaline natural seawater. Even in the high current density of 100 mA·cm^{-2}, the voltages are 1.82 and 1.93 V, respectively. The negligible increase of the voltage in alkaline natural seawater demonstrated Co_3O_4-RuO_2@NCP||Co_3O_4-RuO_2@NCP electrode pair is well able to mitigate these adverse effects and maintain high activity even in challenging natural seawater environments. Besides, chrono-potential test at a constant current density of 10 mA·cm^{-2} (Fig. 4(b)) suggest the activity can be maintained at least of 24 h, proving the excellent stability.

The produced H_2 and O_2 at the Co_3O_4-RuO_2@NCP surface were

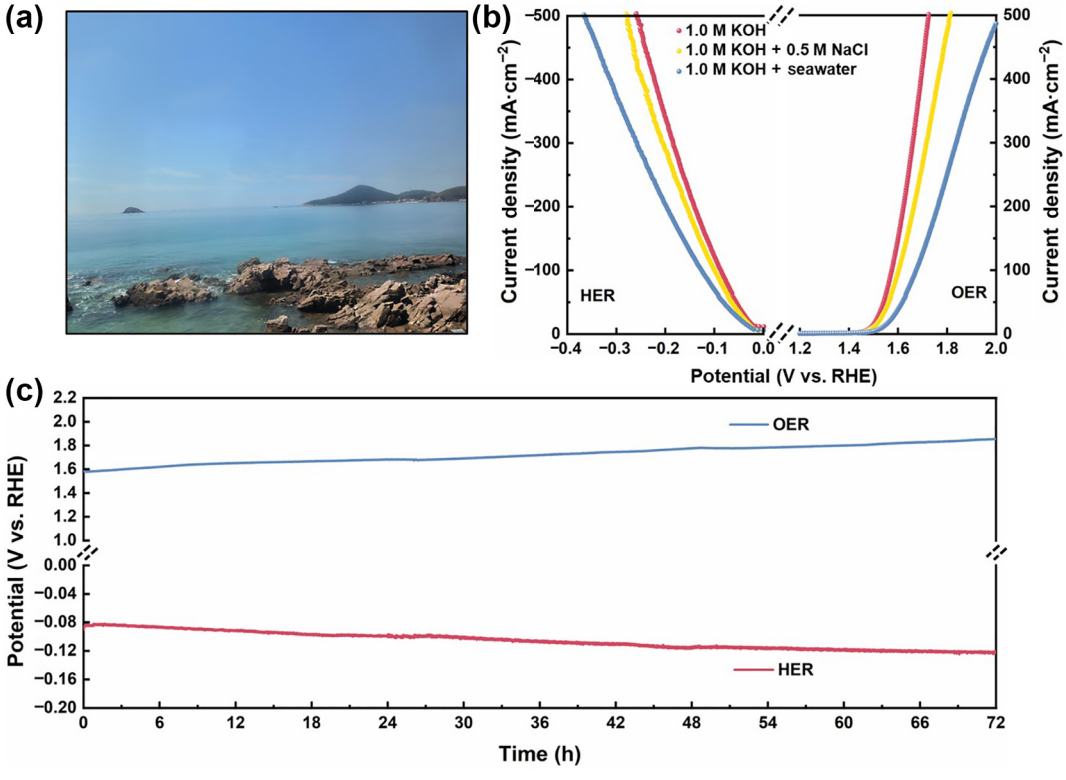

Figure 3 (a) Yellow Sea seawater sampling point, (b) LSV curves for HER and OER, and (c) stability curves.

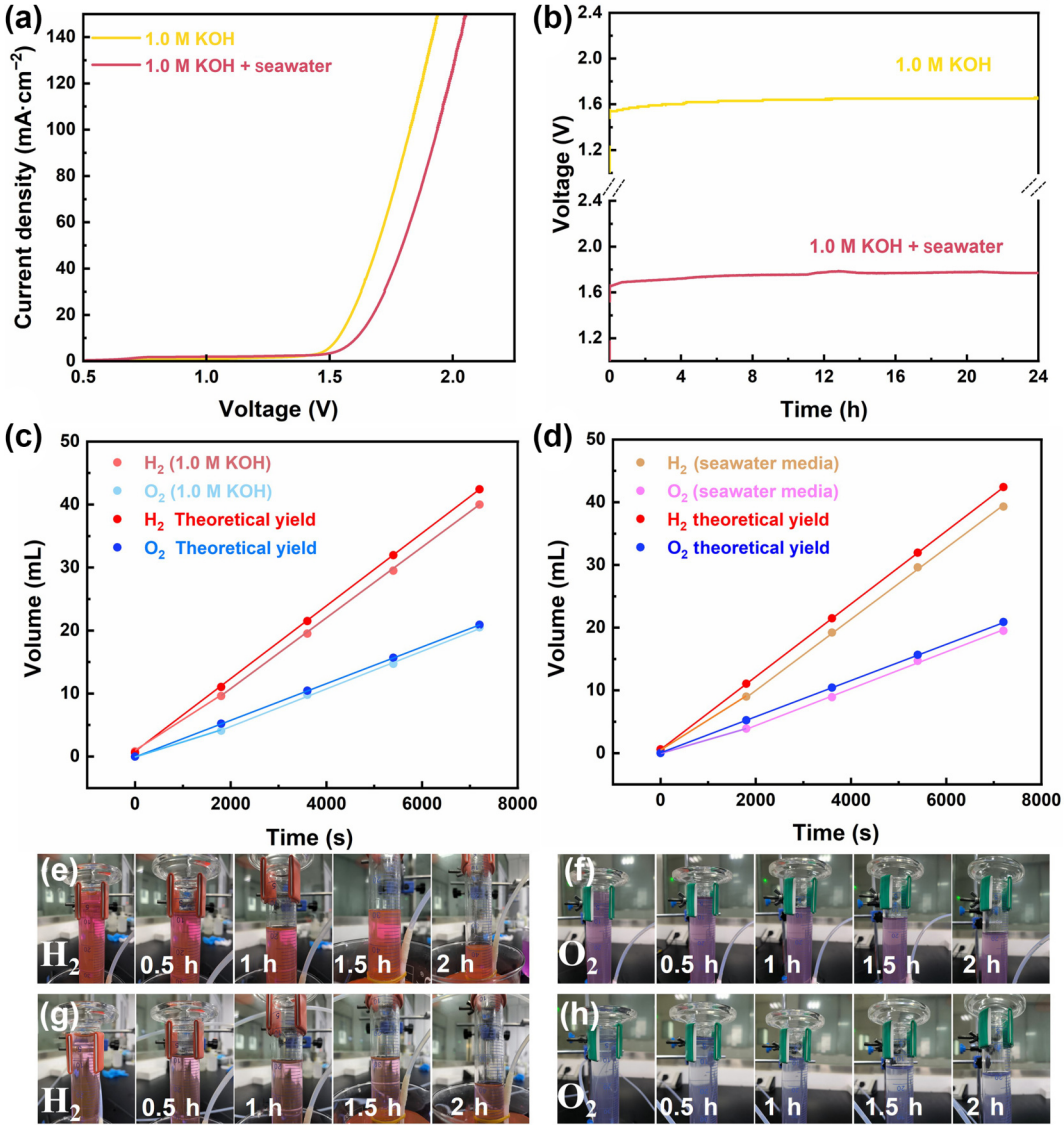

Figure 4 (a) Two-electrode tests for overall water splitting and (b) stability curves. Comparison chart of theoretical and experimental gas production in (c) 1 M KOH and (d) alkaline natural seawater. (e) and (g) Drainage device for H_2 and ((f) and (h)) O_2 collection with different reaction time in alkaline seawater and 1 M KOH.

collected to investigate the Faraday efficiency by draining through an H-type electrolyzer with Nafion membrane as the separator [32]. The comparison chart of theoretical and experimental gas volume was plotted in Figs. 4(c) and 4(d), and the photos in Figs. 4(e)–4(h) show the gas volume at different times. The total amount of H_2 and O_2 released from the device displayed the ratio of H_2:O_2 = 2:1, and the experimentally measured gas amount equals well to the theoretically calculated amount, suggesting high Faradic efficiencies. The amounts of H_2 and O_2 released from the device after 2 h were 40/20.2 mL and 39.8/20 mL in 1 M KOH and alkaline natural seawater, and the Faraday efficiencies were calculated to be 97% and 95%, respectively, suggesting this bifunctional Co_3O_4-RuO_2@NCP catalyst has very high selectivity for catalyzing water electrolysis even in seawater.

2.4 Mechanism study

XPS was performed to investigate the surface chemical composition and bonding states of Co_3O_4-RuO_2@NCP (Fig. 5 and Fig. S9 in the ESM). Figure 5(a) presents the Ru 3p spectra for Co_3O_4-RuO_2@NCP before and after the HER stability test, fresh Co_3O_4-RuO_2@NCP shows characteristic peaks at 462.9 and 485.4 eV, corresponding to the Ru $3p_{3/2}$ and Ru $3p_{1/2}$ binding energies, respectively. Additional peaks at 466.3 and 488.6 eV are identified as satellite peaks [33]. Post-HER stability testing, a negative shift of 0.4 eV in the Ru 3p binding energy suggests partial reduction of Ru^{4+} to Ru^0 at negative potential on the catalyst surface, because the reduction of RuO_2 is thermodynamically preferable compared to HER, and the *in-situ* generated Ru-Co_3O_4 was the active center [34]. Under alkaline conditions, Co_3O_4 first promotes H_2O dissociation into OH^- and H^+ due to the strengthening adsorption of OH^- on Co_3O_4 [35], and then the produced H^+ moved to the Ru sites to form H_2 molecule, thus the HER process in alkali was enhanced significantly [34]. While after OER stability test, the binding energy of Ru 3p spectrum showed a positive shift of 0.3 eV, which is due to the strong interaction between OH^- or other oxygen-containing substances in alkali with Ru species, thereby changing the electronic structure and coordination environment of Ru. This interaction may enhance the electronic coupling between the RuO_2

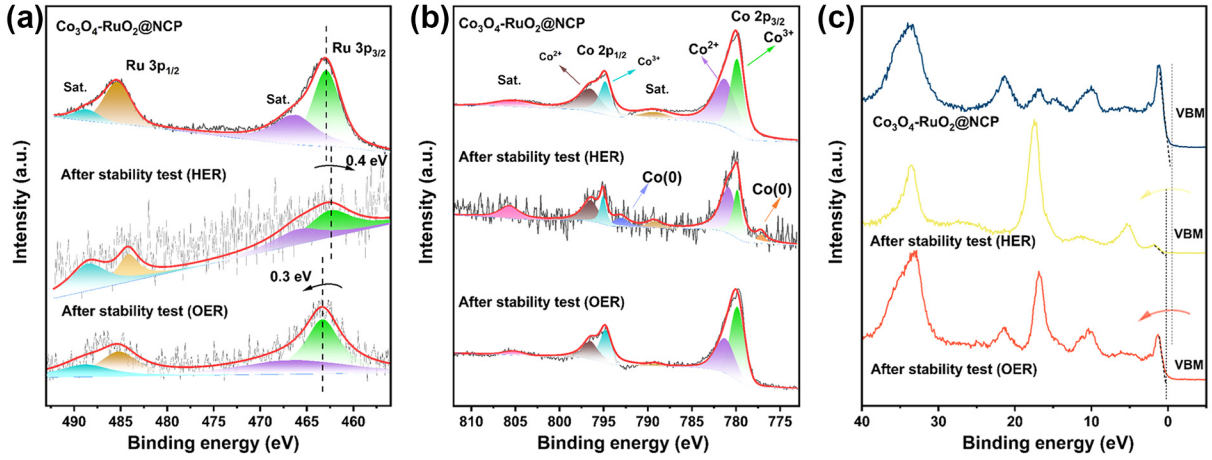

Figure 5 XPS spectra of (a) Ru 3p and (b) Co 2p, and (c) VB spectra of Co_3O_4-RuO_2@NCP.

active site and OH^-, promoting the OER process [36]. The Co 2p spectra (Fig. 5(b)) depict characteristic peaks before and after HER and OER stability test, with peaks at 796.5 and 794.8 eV were ascribed to Co^{2+} and Co^{3+} in Co $2p_{1/2}$, and those at 781.3 and 779.8 eV were ascribed to Co^{2+} and Co^{3+} in Co $2p_{3/2}$, respectively. Satellite peaks at 789.1 and 805.2 eV further validate the multivalent state of Co [37]. As for the Co 2p spectrum after HER, the XPS peaks at low binding energies (777.1 and 793.0 eV) can be assigned to Co(0), and the peak area ratio of Co^{3+}/Co^{2+} decreased compared with the fresh one and the sample after OER test, owning to the reducing environment of the HER.

The VB spectra of Co_3O_4-RuO_2@NCP in Fig. 5(c) illustrate changes in the electronic structure induced by HER and OER processes. Post-HER and OER stability test, a decrease in low-binding-energy VB signal intensity implies potential surface reconfiguration or active phase transitions during the electrocatalytic process, rearranging the valence band structure, potentially forming new peaks or altering peak intensities [38]. Both HER and OER stability tests resulted in intensified peaks around 17 eV in the VB spectrum, likely due to enhanced electronic coupling between Co_3O_4 and RuO_2 during catalysis. This is consistent with observations in polymetallic oxides, where redox-induced electronic coupling produced mixed valence states, the localized electronic density and charge redistribution were enhanced, thereby causing electron density peaks in high-binding-energy regions [39]. Moreover, surface-adsorbed H_{ads} and O_{ads} may further modulate the electronic structure of the catalyst, significantly altering relevant valence band states. Notably, post-HER and OER samples exhibited positive shifts in the valence band maximum (VBM) compared to the fresh one. This shift suggests that Ru site electron modulation reduces H_{ads} adsorption affinity while enhancing O_{ads} adsorption, favoring H_2O dissociation process. These findings highlights an effective electron regulation mechanism in Co_3O_4-RuO_2@NCP, underscoring its potential for efficient electrocatalysis in alkaline media [40].

Furthermore, the models of Co_3O_4-Ru, Co_3O_4-RuO_2 and Co_3O_4-RuO_2@NCP were constructed to verify the mechanism conclusion by DFT calculation [41]. The HER and OER performances of Co_3O_4-Ru and Co_3O_4-RuO_2 under alkaline condition were acquired to prove the reconstruction of the active sites during electrocatalysis (Figs. S10 and S11 in the ESM). Compared to Co_3O_4-RuO_2, the Ru species in Co_3O_4-Ru exhibited a greater ability to adsorb H_2O molecule (−0.54 to −0.18 eV) and dissociate H_2O into H_2 and OH^- (ΔG = 0.88 eV to ΔG = 1.17 eV) under alkaline conditions (Fig. 6(a)), that can be attributed to the stronger metallic properties and higher density of active electrons on Co_3O_4-Ru surface [10], therefore, a conclusion could be draw that the reconstruction of Co_3O_4-RuO_2 into a Co_3O_4-Ru structure facilitates the alkaline HER. Compared with the HER, OER involves a more complex transformation process (Figs. S12 and S13 in the ESM), which entails more than simple electron transfer. On Co_3O_4-RuO_2 surface, the rate-determining step (RDS) for alkaline OER is the conversion of OOH* to O_2 (Fig. 6(b)). A significant reduction in the activation barrier on Co_3O_4-RuO_2 surface (η = 0.50 eV) was accompanied.

Additionally, the nitrogen doped carbon (NC) coated usually leaded to a certain impact on the catalyst [42], and more in-depth DFT calculations were investigated. Difference charge density plots revealed the influence of NC on the electronic structure of the Co_3O_4-RuO_2 system. In contrast to the interactions between Co_3O_4 and RuO_2 within Co_3O_4-RuO_2 structure (Fig. 6(c)), the Co_3O_4-RuO_2@NCP composite displayed additional electron transfer pathways between NC and both Co_3O_4 and RuO_2 components (Fig. 6(d)). Further analysis of surface energy variations via the density of states (DOS) (Fig. S14 in the ESM) revealed that Co_3O_4-RuO_2 exhibited a significant density of states near the Fermi level (E_F = 0 eV). Upon NC coated, the DOS profile undergoes marked alterations due to the electronic structure disparity between NC and the metal oxides. Nevertheless, considerable continuous states persist near E_F, suggesting superior charge transfer properties at the surface [43]. Moreover, qualitative analysis of Ru and Co projected DOS (PDOS) elucidated the electronic modifications in Co_3O_4-RuO_2@NCP. NC coating induced a shift in the Ru d-band center from −1.692 eV in Co_3O_4-RuO_2 to −1.593 eV in Co_3O_4-RuO_2@NCP (Fig. 6(e)). The d-band center in Co_3O_4-RuO_2@NCP was closer to the Fermi level, that attributed to NC-RuO_2 interfacial charge transfer, signified increased surface energy of Ru species [44]. Similarly, the Co d-band center of Co_3O_4-RuO_2@NCP (−1.582 eV) was also closer to Fermi level than that of Co_3O_4-RuO_2 (−1.676 eV) (Fig. 6(f)), demonstrating that NC similarly modulates the Co surface electronic environment towards higher energy. Furthermore, Bader charge analysis revealed the charge number over Ru and Co species quantitatively (Table S2 in the ESM). Consistent with the PDOS results, the electron transformation between NC and RuO_2, Co_3O_4 effectively increased the electron density of the Ru and Co atoms.

Moreover, the formation of the Co_3O_4-RuO_2@NCP imparts a

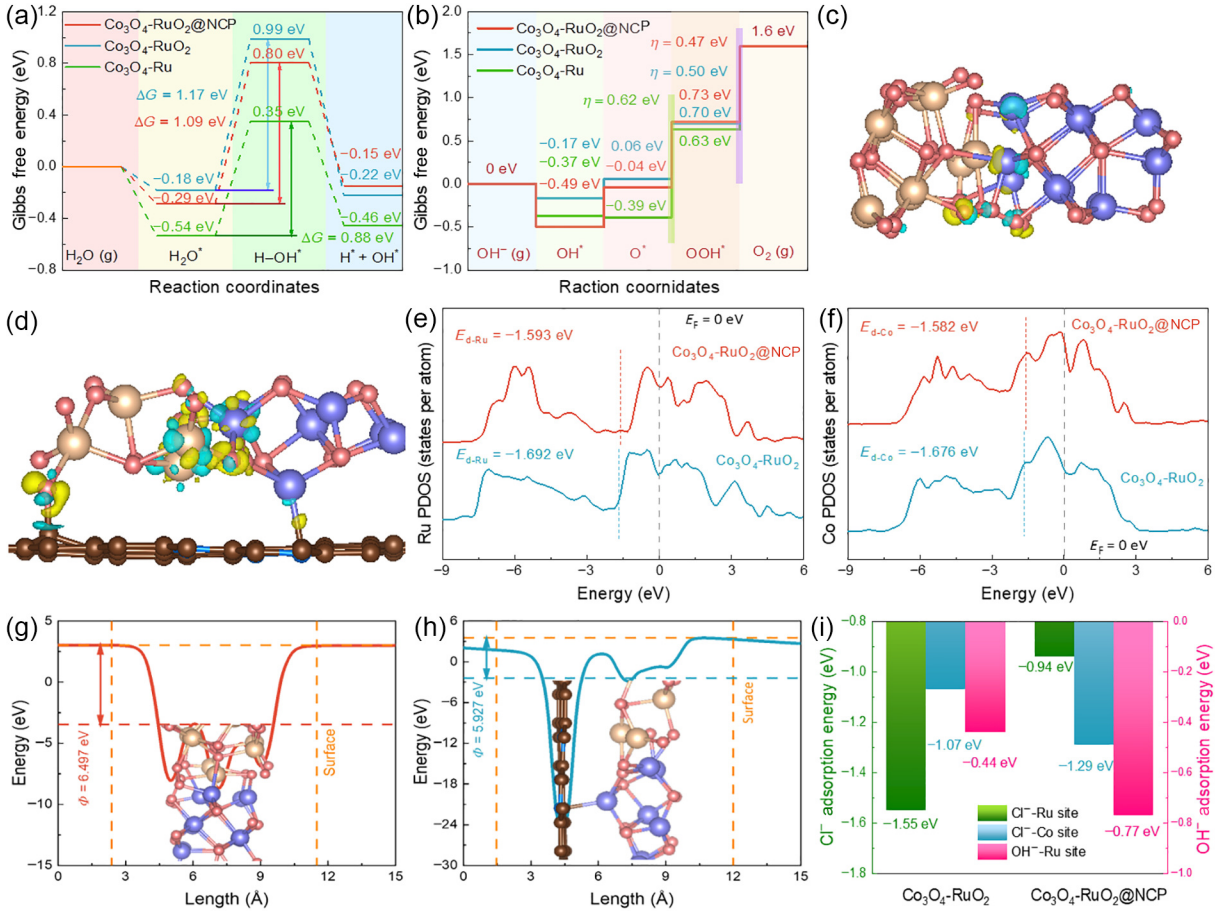

Figure 6 Free energy paths of (a) HER and (b) OER on Co_3O_4-Ru, Co_3O_4-RuO_2, Co_3O_4-RuO_2@NCP. Charge density difference plot of (c) Co_3O_4-RuO_2 and (d) Co_3O_4-RuO_2@NCP, the isosurface value is 0.005 e·bohr^{-3}. (e) Ru and (f) Co PDOS, and (g) and (h) work function of Co_3O_4-RuO_2 and Co_3O_4-RuO_2@NCP. (i) Cl^- and OH^- adsorption energy of Co_3O_4-RuO_2 and Co_3O_4-RuO_2@NCP.

significant influence on the surface catalytic properties. The work function of Co_3O_4-RuO_2 (6.497 eV) (Fig. 6(g)) was substantially higher than that of Co_3O_4-RuO_2@NCP (5.927 eV) (Fig. 6(h)), indicating that the electrons on the Co_3O_4-RuO_2@NCP surface were more readily mobilized to participate in catalytic reactions, that could be attributable to the formation of the heterojunction structure and the increased electron density on the Co_3O_4 and RuO_2 surfaces. Additionally, the elevated surface energy of Ru and Co species correlated with enhanced alkaline HER performance in Co_3O_4-RuO_2@NCP (Fig. S15 in the ESM). The HER energy barrier decreases from ΔG = 1.17 eV (Co_3O_4-RuO_2) to ΔG = 1.09 eV (Co_3O_4-RuO_2@NCP), that remained higher than that of Co_3O_4-Ru. It suggested that the HER activity on Co_3O_4-RuO_2@NCP also relies on the reconstruction of active sites during the reaction process. In contrast to the alkaline HER, the OER performance of Co_3O_4-RuO_2@NCP closely mirrors that of Co_3O_4-RuO_2, due to structural similarities (Fig. S16 in the ESM). Both Co_3O_4-RuO_2 and Co_3O_4-RuO_2@NCP catalysts possessed identical RDS, the conversion of OOH to O_2, and the similar reaction energy barriers (η = 0.47 eV and η = 0.50 eV).

To decipher the mechanistic basis for performance enhancement in seawater media, Cl^- adsorption energies were calculated for specific sites on the catalyst surfaces (Fig. S17 in the ESM). Strong chemisorption of Cl^- occurs on Co_3O_4-RuO_2 (Fig. 6(i)), with Ru sites exhibiting higher Cl^- binding affinity (−1.55 eV) than Co sites (−1.07 eV), thereby impeding OH^- adsorption (−0.44 eV) at catalytically critical Ru sites. Upon NC incorporation (Co_3O_4-RuO_2@NCP), the increased Ru electron density weakens Cl^- adsorption on Ru sites, lowering its energy to −0.94 eV. Crucially, the energy difference governing Cl^- vs. OH^- adsorption preference on Ru sites narrows dramatically from 1.11 eV (Co_3O_4-RuO_2) to 0.17 eV (Co_3O_4-RuO_2@NCP). Consequently, the competitive adsorption equilibrium is optimized, directly inhibited the CER, accounting for the superior seawater OER activity.

3 Conclusions

In summary, a novel N-doped carbon polyhedral encapsulated Co_3O_4-RuO_2 heterostructure with bifunctional catalytic activity was synthesized through a "template-assistance-self-assembly-pyrolysis" strategy, in which ZIF-67 and g-C_3N_4 were used to anchor and disperse the Ru metal. Electrochemical test results showed that Co_3O_4-RuO_2@NCP not only displayed good bifunctional electrocatalytic performance in alkali, even in the alkaline simulated seawater and alkaline natural seawater, there is also no significant activity degradation. When assembled into a two-electrode system for overall water splitting, Co_3O_4-RuO_2@NCP couple can achieve 10 mA·cm^{-2} at a low cell voltage of 1.60 V, 100 mA·cm^{-2} at 1.93 V in alkaline natural seawater, with good long-term durability as well as high Faraday efficiency. Through investigating the XPS and VB before and post the electrocatalytic process, partial reduction of Ru^{4+} to Ru(0) in HER process, thus Ru-Co_3O_4 was the active center, while in the OER process, the valence state of Ru species was

further increased, indicating the intense interaction between OH^-, which would benefit the OER process. VB also suggested the localized electronic density and charge redistribution were enhanced during the HER and OER process, and the Ru sites played a key role in the H_{ads} adsorption and O_{ads} adsorption. DFT calculations revealed the reconstruction of the active sites and the electron interaction between NC and Co_3O_4-RuO_2 structure during electrocatalysis optimized the adsorption and activation process of key active species. Following the formation of the Co_3O_4-RuO_2 heterojunction structure, the electron density on the Co_3O_4-RuO_2 surface increases, rendering the electron more readily activated to participate in reactions, that consequently enhances the catalytic activity of Co_3O_4-RuO_2@NCP towards both the alkaline HER and OER. Furthermore, the modulation of the Co_3O_4-RuO_2 @NCP surface electronic structure by NC improves the competitive adsorption between Cl^- and OH^-, thereby significantly enhancing the catalytic selectivity of Co_3O_4-RuO_2 @NCP in seawater. The research conclusion in this work suggested the Ru-Co based polymetallic oxides had promising application potential for electrochemical natural seawater splitting.

Electronic Supplementary Material: Supplementary material (experimental methods, theoretical calculation methods, supplementary data figures and tables, etc.) is available in the online version of this article at https://doi.org/10.26599/NR.2026.94908487.

Data availability

All data needed to support the conclusions in the paper are presented in the manuscript and the Electronic Supplementary Material. Additional data related to this paper may be requested from the corresponding author upon request.

Acknowledgements

This work was supported by the National Natural Science Foundation of China (Nos. 22109090, 22478432, 22522819, and 22406191), Shandong Provincial Natural Science Foundation (Nos. ZR2024QB031, ZR2024JQ004, and ZR2025QC98), the Taishan Scholars Program of Shandong Province, and the National Defense Science and Technology Innovation Project, National Key Research and Development Program of China (No. 2025YFE0126400).

Declaration of competing interest

All the contributing authors report no conflict of interests in this work.

Author contribution statement

Y. L.: Conceptualization, methodology, investigation, writing – original draft. P. X. L., Z. H. W., Z. C. L., J. N. G., and Y. Y. L.: Formal analysis, data collection and curation, visualization. X. Y.: Funding acquisition, project administration. C. F.: Supervision, writing – review & editing, theoretical analysis. Y. P.: Supervision, funding acquisition, writing – review & editing. All authors have read and agreed to the published version of the manuscript.

Use of AI statement

None.

References

[1] Dresp, S.; Dionigi, F.; Loos, S.; de Araujo, J. F.; Spöri, C.; Gliech, M.; Dau, H.; Strasser, P. Direct electrolytic splitting of seawater: Activity, selectivity, degradation, and recovery studied from the molecular catalyst structure to the electrolyzer cell level. *Adv. Energy Mater.* **2018**, *8*, 1800338.

[2] Zhao, G. Q.; Rui, K.; Dou, S. X.; Sun, W. P. Heterostructures for electrochemical hydrogen evolution reaction: A review. *Adv. Funct. Mater.* **2018**, *28*, 1803291.

[3] Hodgson, A.; Haq, S. Water adsorption and the wetting of metal surfaces. *Surf. Sci. Rep.* **2009**, *64*, 381–451.

[4] Guo, Y. J.; Shi, L.; Shi, X. S.; Zhao, T. T.; Tian, W. C.; Zhang, S. L.; Liu, D.; Li, Y. Z.; Zhong, F. P.; Zhao, S. L. Scalable metal-organic framework-based electrodes for efficient alkaline water electrolysis. *Nat. Chem. Eng.* **2025**, *2*, 474–483.

[5] Li, J.; Xie, F. X.; Pang, W. W.; Liang, Q. Y.; Yang, X. F.; Zhang, L. Regulate transportation of ions and polysulfides in all-solid-state Li–S batteries using ordered-MOF composite solid electrolyte. *Sci. Adv.* **2024**, *10*, eadl3925.

[6] Pan, Y.; Sun, K. A.; Liu, S. J.; Cao, X.; Wu, K. L.; Cheong, W. C.; Chen, Z.; Wang, Y.; Li, Y.; Liu, Y. Q. et al. Core-shell ZIF-8@ZIF-67-derived CoP nanoparticle-embedded N-doped carbon nanotube hollow polyhedron for efficient overall water splitting. *J. Am. Chem. Soc.* **2018**, *140*, 2610–2618.

[7] Song, H. Q.; Cheng, Y. J.; Li, B. J.; Fan, Y. P.; Liu, B. Z.; Tang, Z. Y.; Lu, S. Y. Carbon dots and RuP_2 nanohybrid as an efficient bifunctional catalyst for electrochemical hydrogen evolution reaction and hydrolysis of ammonia borane. *ACS Sustainable Chem. Eng.* **2020**, *8*, 3995–4002.

[8] Liu, Y.; Li, X.; Zhang, Q. H.; Li, W. D.; Xie, Y.; Liu, H. Y.; Shang, L.; Liu, Z. Y.; Chen, Z. M.; Gu, L. et al. A general route to prepare low-ruthenium-content bimetallic electrocatalysts for pH-universal hydrogen evolution reaction by using carbon quantum dots. *Angew. Chem., Int. Ed.* **2020**, *59*, 1718–1726.

[9] Zhu, X. L.; Wang, P.; Wang, Z. Y.; Liu, Y. Y.; Zheng, Z. K.; Zhang, Q. Q.; Zhang, X. Y.; Dai, Y.; Whangbo, M.-H.; Huang, B. B. Co_3O_4 nanobelt arrays assembled with ultrathin nanosheets as highly efficient and stable electrocatalysts for the chlorine evolution reaction. *J. Mater. Chem. A* **2018**, *6*, 12718–12723.

[10] Wang, M. M.; Feng, C.; Mi, W. L.; Guo, M. D.; Guan, Z. K.; Li, M.; Chen, H. C.; Liu, Y. Q.; Pan, Y. Defect-induced electron redistribution between Pt–N_3S_1 single atomic sites and Pt clusters for synergistic electrocatalytic hydrogen production with ultra-high mass activity. *Adv. Funct. Mater.* **2024**, *34*, 2309474.

[11] Xiang, J. X.; Zhou, F. H.; Ma, X. X.; Wu, J.; Guo, C. J.; Qi, Y. M.; Yu, J. L.; Fan, W. K.; Fang, W. J.; Li, K. et al. Spherical cluster heterojunction engineering of NiFeP/g-C_3N_4 for efficient oxygen evolution reaction in alkaline solution. *J. Colloid Interface Sci.* **2024**, *674*, 266–278.

[12] Walton, K. S.; Snurr, R. Q. Applicability of the BET method for determining surface areas of microporous metal-organic frameworks. *J. Am. Chem. Soc.* **2007**, *129*, 8552–8556.

[13] Ambroz, F.; Macdonald, T. J.; Martis, V.; Parkin, I. P. Evaluation of the BET theory for the characterization of meso and microporous MOFs. *Small Methods* **2018**, *2*, 1800173.

[14] Raduwan, N. F.; Shaari, N.; Kamarudin, S. K.; Masdar, M. S.; Yunus, R. M. Structural transformation doubly triggered by hydrothermal temperature and reaction time in 3D mixed transition metal oxide: Great enhancement of pore size distribution and specific surface area. *Int. J. Hydrogen Energy* **2023**, *48*, 27289–27297.

[15] Li, L.; Wang, S.; Xiong, L. F.; Wang, B.; Yang, G.; Yang, S. C. Surface-engineered mesoporous Pt nanodendrites with Ni dopant for highly enhanced catalytic performance in hydrogen evolution reaction. *J. Mater. Chem. A* **2019**, *7*, 12800–12807.

[16] Zhou, B. H.; Gao, R. J.; Zou, J. J.; Yang, H. M. Surface design strategy of catalysts for water electrolysis. *Small* **2022**, *18*, 2202336.

[17] Chen, D.; Yu, R. H.; Wu, D. L.; Zhao, H. Y.; Wang, P. Y.; Zhu, J. W.; Ji, P. X.; Pu, Z. H.; Chen, L.; Yu, J. et al. Anion-modulated molybdenum oxide enclosed ruthenium nano-capsules with almost the same water splitting capability in acidic and alkaline media. *Nano Energy* **2022**, *100*, 107445.

[18] Liu, N.; Zhai, Z. H.; Yu, B.; Yang, W. F.; Cheng, G. H.; Zhang, Z. H. Bifunctional nanoporous ruthenium-nickel alloy nanowire electrocatalysts towards oxygen/hydrogen evolution reaction. *Int. J. Hydrogen Energy* **2022**, *47*, 31330–31341.

[19] Zhang, Z. F.; Wang, H. Q.; Ma, M. J.; Liu, H. L.; Zhang, Z. C.; Zhou, W. J.; Liu, H. Integrating NiMoO wafer as a heterogeneous 'turbo' for engineering robust Ru-based electrocatalyst for overall water splitting. *Chem. Eng. J.* **2021**, *420*, 127686.

[20] Li, M. X.; Wang, H. Y.; Zhu, W. D.; Li, W. M.; Wang, C.; Lu, X. F. RuNi nanoparticles embedded in N-doped carbon nanofibers as a robust bifunctional catalyst for efficient overall water splitting. *Adv. Sci.* **2020**, *7*, 1901833.

[21] Li, G. N.; Zheng, K. T.; Li, W. S.; He, Y. C.; Xu, C. J. Ultralow Ru-induced bimetal electrocatalysts with a Ru-enriched and mixed-valence surface anchored on a hollow carbon matrix for oxygen reduction and water splitting. *ACS Appl. Mater. Interfaces* **2020**, *12*, 51437–51447.

[22] Lin, X. L.; Liu, J. L.; Qiu, X. Q.; Liu, B. W.; Wang, X. F.; Chen, L. H.; Qin, Y. L. Ru–FeNi alloy heterojunctions on lignin-derived carbon as bifunctional electrocatalysts for efficient overall water splitting. *Angew. Chem., Int. Ed.* **2023**, *62*, e202306333.

[23] Liu, W. X.; Que, W. B.; Yin, R. L.; Dai, J. L.; Zheng, D.; Feng, J. X.; Xu, X. L.; Wu, F. F.; Shi, W. H.; Liu, X. J. et al. Ferrum-molybdenum dual incorporated cobalt oxides as efficient bifunctional anti-corrosion electrocatalyst for seawater splitting. *Appl. Catal. B: Environ.* **2023**, *328*, 122488.

[24] Xue, Y. Q.; Yan, Q.; Bai, X. J.; Xu, Y. Y.; Zhang, X.; Li, Y. J.; Zhu, K.; Ye, K.; Yan, J.; Cao, D. X. et al. Ruthenium-nickel-cobalt alloy nanoparticles embedded in hollow carbon microtubes as a bifunctional mosaic catalyst for overall water splitting. *J. Colloid Interface Sci.* **2022**, *612*, 710–721.

[25] Zhao, S. L.; Ran, S. Y.; Shi, N.; Liu, M. L.; Sun, W.; Yu, Y.; Zhu, Z. H. Structural design induced electronic optimization in single-phase MoCoP nanocrystal for boosting oxygen reduction, oxygen evolution, and hydrogen evolution. *Small* **2023**, *19*, 2302414.

[26] Huang, K.; Xia, J. Y.; Lu, Y.; Zhang, B. W.; Shi, W. C.; Cao, X.; Zhang, X. Y.; Woods, L. M.; Han, C. C.; Chen, C. J. et al. Self-reconstructed spinel surface structure enabling the long-term stable hydrogen evolution reaction/oxygen evolution reaction efficiency of FeCoNiRu high-entropy alloyed electrocatalyst. *Adv. Sci.* **2023**, *10*, 2300094.

[27] Zhang, P. F.; Liu, Y. D.; Liang, T. T.; Ang, E. H.; Zhang, X.; Ma, F.; Dai, Z. F. Nitrogen-doped carbon wrapped Co–Mo_2C dual Mott–Schottky nanosheets with large porosity for efficient water electrolysis. *Appl. Catal. B: Environ.* **2021**, *284*, 119738.

[28] Li, W. J.; Deng, Y. Q.; Luo, L.; Du, Y. S.; Cheng, X. H.; Wu, Q. Nitrogen-doped Fe_2O_3/$NiTe_2$ as an excellent bifunctional electrocatalyst for overall water splitting. *J. Colloid Interface Sci.* **2023**, *639*, 416–423.

[29] Zhang, F. H.; Yu, L.; Wu, L. B.; Luo, D.; Ren, Z. F. Rational design of oxygen evolution reaction catalysts for seawater electrolysis. *Trends Chem.* **2021**, *3*, 485–498.

[30] Xie, H. P.; Zhao, Z. Y.; Liu, T.; Wu, Y. F.; Lan, C.; Jiang, W. C.; Zhu, L. Y.; Wang, Y. P.; Yang, D. S.; Shao, Z. P. A membrane-based seawater electrolyser for hydrogen generation. *Nature* **2022**, *612*, 673–678.

[31] Na, J.; Yu, H. M.; Jia, S. Y.; Chi, J.; Lv, K. Q.; Li, T. Z.; Zhao, Y.; Zhao, Y. T.; Zhang, H. T.; Shao, Z. G. Electrochemical reconstruction of non-noble metal-based heterostructure nanorod arrays electrodes for highly stable anion exchange membrane seawater electrolysis. *J. Energy Chem.* **2024**, *91*, 370–382.

[32] Kempler, P. A.; Nielander, A. C. Reliable reporting of Faradaic efficiencies for electrocatalysis research. *Nat. Commun.* **2023**, *14*, 1158.

[33] Gao, Y. X.; Zheng, D. B.; Li, Q. C.; Xiao, W. P.; Ma, T. Y.; Fu, Y. L.; Wu, Z. X.; Wang, L. 3D Co_3O_4–RuO_2 hollow spheres with abundant interfaces as advanced trifunctional electrocatalyst for water-splitting and flexible Zn-air battery. *Adv. Funct. Mater.* **2022**, *32*, 2203206.

[34] Zhang, H. M.; Lv, Y.; Chen, C.; Lv, C. W.; Wu, X. Y.; Guo, J. X.; Jia, D. Z. Inter-doped ruthenium-nickel oxide heterostructure nanosheets with dual active centers for electrochemical-/solar-driven overall water splitting. *Appl. Catal. B: Environ.* **2021**, *298*, 120611.

[35] Man, I. C.; Su, H. Y.; Calle-Vallejo, F.; Hansen, H. A.; Martínez, J. I.; Inoglu, N. G.; Kitchin, J.; Jaramillo, T. F.; Nørskov, J. K.; Rossmeisl, J. Universality in oxygen evolution electrocatalysis on oxide surfaces. *ChemCatChem* **2011**, *3*, 1159–1165.

[36] Yang, C. D.; Wu, Z. H.; Zhao, Z. Y.; Gao, Y.; Ma, T.; He, C.; Wu, C. Z.; Liu, X. K.; Luo, X. L.; Li, S. et al. Electronic structure-dependent water-dissociation pathways of ruthenium-based catalysts in alkaline H_2-evolution. *Small* **2023**, *19*, 2206949.

[37] Shahzad, A.; Zulfiqar, F.; Nadeem, M. A. Cobalt containing bimetallic ZIFs and their derivatives as OER electrocatalysts: A critical review. *Coord. Chem. Rev.* **2023**, *477*, 214925.

[38] Naamneh, M.; Guedes, E. B.; Prakash, A.; Cardoso, H. M.; Shi, M.; Plumb, N. C.; Brito, W. H.; Jalan, B.; Radović, M. Low-dimensional electronic state at the surface of a transparent conductive oxide. *Commun. Phys.* **2022**, *5*, 317.

[39] Fu, W. W.; Wang, Y. W.; Hu, J. S.; Zhang, H. J.; Luo, P.; Sun, F.; Ma, X. G.; Huang, Z. Y.; Li, J.; Guo, Z. P. et al. Surface-electron coupling for efficient hydrogen evolution. *Angew. Chem., Int. Ed.* **2019**, *58*, 17709–17717.

[40] Su, J. W.; Ge, R. X.; Jiang, K. M.; Dong, Y.; Hao, F.; Tian, Z. Q.; Chen, G. X.; Chen, L. Assembling ultrasmall copper-doped ruthenium oxide nanocrystals into hollow porous polyhedra: Highly robust electrocatalysts for oxygen evolution in acidic media. *Adv. Mater.* **2018**, *30*, 1801351.

[41] Feng, C.; Xiong, G. Y.; Chen, C.; Lin, Y.; Wang, Z.; Lu, Y. K.; Liu, F.; Li, X. B.; Liu, Y. Q.; Zhang, R. D. et al. Highly dispersed Pt/Co_3O_4 catalyst constructed by vacancy defect inductive effect for enhanced catalytic propane total oxidation. *Chin. J. Catal.* **2025**, *75*, 21–33.

[42] Huang, Z. D.; Cao, S. F.; Feng, C.; Li, Y. C.; Liang, Y. C.; Li, X. L.; Mei, H.; Fan, W. D.; Ben Xu, N.; Yuan, S. et al. Polydopamine bridging strategy enables pseudomorphic transformation of multi-component MOFs into ultrasmall NiSe/WSe_2@NC heterojunctions for enhanced alkaline hydrogen evolution. *Appl. Catal. B: Environ.* **2023**, *334*, 122769.

[43] Feng, C.; Gao, Q. Q.; Xiong, G. Y.; Chen, Y. F.; Pan, Y.; Fei, Z. Y.; Li, Y. P.; Lu, Y. K.; Liu, C. G.; Liu, Y. Q. Defect engineering technique for the fabrication of $LaCoO_3$ perovskite catalyst via urea treatment for total oxidation of propane. *Appl. Catal. B: Environ.* **2022**, *304*, 121005.

[44] Feng, C.; Chen, C.; Xiong, G. Y.; Yang, D.; Wang, Z.; Pan, Y.; Fei, Z. Y.; Lu, Y. K.; Liu, Y. Q.; Zhang, R. D. et al. Cr-doping regulates Mn_3O_4 spinel structure for efficient total oxidation of propane: Structural effects and reaction mechanism determination. *Appl. Catal. B: Environ.* **2023**, *328*, 122528.